

Technical Report

TR-2015-010

A Patient-Specific Follow Up Study of the Impact of Thoracic Endovascular Repair (TEVAR) on Aortic Anatomy and on Post-Operative Hemodynamic

by

Diego Gallo, Adrien Lefieux, Simone Morganti, Alessandro Veneziani, Alessandro Reali,
Ferdinando Auricchio, Michele Conti, Umberto Morbiducci

MATHEMATICS AND COMPUTER SCIENCE

EMORY UNIVERSITY

A Patient-Specific Follow Up Study of the Impact of Thoracic Endovascular Repair (TEVAR) on Aortic Anatomy and on Post-Operative Hemodynamics.

Diego Gallo¹, Adrien Lefieux², Simone Morganti², Alessandro Veneziani³,
Alessandro Reali^{2*}, Ferdinando Auricchio², Michele Conti², Umberto Morbiducci¹

1 Department of Mechanical and Aerospace Engineering, Politecnico di Torino, Turin, Italy

2 Department of Civil Engineering and Architecture, University of Pavia, Pavia, Italy

3 Department of Mathematics and Computer Science, Emory University, Atlanta, GA, USA

Corresponding Author:

Alessandro Reali (alessandro.reali@unipv.it)

Department of Civil Engineering and Architecture, University of Pavia
via Ferrata 3, 27100, Pavia, Italy

Abstract

Thoracic endovascular repair (TEVAR) is a minimally invasive alternative to classical open-chest surgery for pathologies of thoracic aorta such as aneurysms or dissections. It consists of the deployment of one or more endografts to either exclude aneurysms pressurization or seal entry tears of dissection. It is a minimally invasive procedure, yet long-term efficacy is still to be demonstrated and analyzed, depending on the geometry and the consequent hemodynamics and remodeling induced by the intervention. In this paper we consider a TEVAR patient by an extensive computational analysis of pre-op, post-op and one-year follow up data. We focus on both geometrical features like curvature, torsion and area variations, as well as on flow-related quantities like Time Average Wall Shear Stress (TAWSS), Oscillatory Shear Index (OSI) and Helicity. Comparison of the different morphologies indicate a partial restoration of normal flow in the region of interest, even though low WSS are still present with the associated risks. Overall, this study demonstrates the efficacy of quantitative computational tools in understanding the long-term impact of TEVAR.

Keywords – Bird beak configuration, morphometry, computational fluid dynamics, wall shear stress, helicity, thoracic aorta.

Introduction

Thoracic aorta is the anatomical portion of the aorta - the main artery of human circulatory system - ranging from the aortic valve to the level of the diaphragm. This region also includes supra-aortic branches supplying brain circulation and it has a key role in the whole circulatory system, integrating the cardiac function by acting as a secondary pump. For these reasons, thoracic aortic diseases, such as aneurysm or dissection, could have dramatic outcomes. Unfortunately, thoracic aortic diseases still remain a global health burden [1], although dramatic progresses have been done in both prevention and treatment, such as thoracic endovascular repair (TEVAR), which is a minimally invasive alternative to classical open-chest surgery. In detail, TEVAR has the final goals (1) to exclude aneurysm pressurization, thus minimizing the risk of rupture, and (2) to seal the proximal entry tear of dissection, triggering a positive remodeling of the diseased aorta. Technically, TEVAR is performed by the endovascular delivery and deployment into the diseased site of one or two endografts, i.e., self-expanding prostheses made of a nitinol scaffold covered by a polymeric skirt. On one hand the use of TEVAR is encouraged by its unquestionable low invasiveness, on the other one the insufficient knowledge of its long term efficacy is still a matter of clinical debate [2]. One of the most frequent causes for early and late stent-graft treatment failure is the anatomical complexity of the aortic arch [3]. In particular, one of the extremities of the device lands at the level of the aortic arch: in case of angulated arches, the stent-graft cannot conform to the arch shape due to its stiffness, resulting in a only partial contact with the aortic wall (malapposition). The lack of apposition of the device to the aortic wall along the arch inner curvature results in the so-called *bird-beak configuration*, consisting in a wedge-shape gap between the undersurface of the stent-graft and the aortic wall [3]. This configuration affects the clinical outcome after TEVAR, being associated with endoleak, stent-graft collapse and infolding [3].

For treatment planning and long-term outcomes of TEVAR, a crucial role is played by (1) vascular morphology, and (2) the consequent hemodynamics, that is majorly affected by the anatomy. Thus, the investigation of TEVAR impact on aortic morphology and hemodynamics over time is of paramount importance. Recently, Midulla et al. [4] have analyzed the TEVAR-induced geometrical changes of the aorta by collecting and analyzing CT pre- and post-operative acquisitions of 30 consecutive patients treated by TEVAR. More quantitative morphometric analyses have been developed to characterize the geometry of healthy vessels or to aid endovascular device design [4-6]. As for a well consolidated procedure, the

appropriate processing of images followed by computational fluid dynamics (CFD) allows to simulate intravascular hemodynamics to obtain highly resolved blood flow patterns (in space and in time) in patient-specific geometric models. For example, recent studies [7-11] investigated some of the consequences of TEVAR on local hemodynamics immediately after stent-graft implantation resorting to patient-specific computations, mainly focusing on the consequence of possible drawbacks of the surgery.

In the present study, we aim at evaluating for the first time a one year follow up study in a real clinical case presenting a bird-beak configuration after TEVAR. In detail, local vascular geometric features like curvature, torsion and area variations are evaluated in the pre-operative geometry and in two post-operative geometries, immediately after the intervention and after one year. In the post-operative geometries, numerical hemodynamic simulations are performed. Both near-wall and intravascular flow quantities are considered and related to the geometric changes, to explore the complex interplay between vascular morphology and hemodynamic and its consequences on aortic remodeling.

Materials and Methods

The image-based workflow applied to study how anatomic attributes and hemodynamics vary in the follow-up study is illustrated in this section. We briefly document the clinical protocol and introduce our aortic lumen segmentation strategy. Then the computational setting to perform vascular geometric characterization and computational hemodynamics is presented.

Image-based anatomical models reconstruction

A 51-years old male subject suffering from an asymptomatic post-dissecting thoracic aortic aneurysm was selected for endovascular exclusion. As detailed elsewhere [7], two cTAG stent-grafts (conformable TAG, W.L. GORE & Associates. Inc., Flagstaff, Arizona, USA), sized 34–34–20 and 28–28–15 mm, were selected for implantation. While six month follow-up imaging confirmed the successful exclusion of the aneurysm without endoleak, immediate post-operative imaging clearly highlighted a bird-beak configuration of the proximal prosthesis [7].

Multislice computed tomography (MSCT) was used at three different stages: (1) pre-operative scan performed few days before the surgery (CASE 0); (2) post-operative scan performed immediately after the surgery (CASE A); (3) post-operative scan performed one year after the surgical intervention (CASE B).

Briefly, MSCT was performed, before and after intravenous administration of 100 mL of iodinated contrast material, using a 16-slice unit (150 mAs, 110kVp; acquisition thickness 5 mm, pitch 1.5; reconstruction thickness 1.2 mm), as previously detailed [7]. According to a previously proposed approach (for the interested reader, details regarding the patient and the effective protocol regarding the extraction of the geometries are presented in [5,7]), image segmentation of the three MSCT image datasets and three-dimensional models reconstruction were performed using the open-source software ITK-Snap [13], with attention used to properly consider the presence of the stent-grafts in CASE A and CASE B.

Phase contrast MRI was performed one year after the intervention on CASE B using the 1.5T scanner Magnetom Sonata Maestro Class (Siemens, Erlangen, Germany, see [7] for details). In this way the flow rate waveform along the cardiac cycle at an aortic cross-section distal to the aortic valve was obtained, suitable to be used as realistic inflow boundary condition to simulate local aortic hemodynamics (as will be clarified in the following).

On the reconstructed realistic three-dimensional geometries of the subject at the pre-operative stage and at two successive post-operative stages, geometric and hemodynamic characterization was performed.

Geometric Quantitative Description

Geometric attributes of the aorta and its branches at the three observational stages were considered for comparison. These attributes are based upon the definition of vessels centerline \mathbf{C} as the geometrical locus of the centers of the maximal inscribed spheres in the vascular geometry [13].

In detail, from the 3D surface triangulation of each anatomic model a discrete set of points forming the centerlines were generated automatically using the open-source Vascular Modeling ToolKit (VMTK, www.vmtk.org). Then, we adopted the 3D free-knots regression splines to represent in closed form the continuous centerlines [14]. This choice allowed the reliable calculation of a set of vascular anatomic features, by filtering the noise in the discrete observations of curves \mathbf{C} . In fact, as described elsewhere [15,16], an order m free-knots regression spline in three dimensions is a piecewise polynomial of degree $m-1$,

with continuous derivatives of order $m-2$ at the knots, whose number and position is not fixed in advance but chosen in a way to minimize a penalized sum of squared error criterion [17]. By properly setting the value for m , we obtained (1) an analytical representation of the centerlines continuous up to the derivatives of order 4, and (2) the quantification of their curvature and torsion by differentiation. In general, we remind that curvature κ and the torsion τ of a curve \mathbf{C} along the curvilinear abscissa s are defined [13,15] as:

$$\begin{aligned}\kappa(s) &= \frac{|\mathbf{C}'(s) \times \mathbf{C}''(s)|}{|\mathbf{C}'(s)|^3} \\ \tau(s) &= \frac{[\mathbf{C}'(s) \times \mathbf{C}''(s)] \cdot \mathbf{C}'''(s)}{|\mathbf{C}'(s) \times \mathbf{C}''(s)|^2}\end{aligned}\quad (1)$$

where primes denote derivatives of curve \mathbf{C} with respect to the curvilinear abscissa s . As definitions state, curvature κ is the reciprocal of the radius of the circle lying on the osculating plane (i.e. the plane defined by the normal and tangent vector to the curve at each point), while torsion τ measures the deviation of the curve from the osculating plane. Over each vascular segment of generic length L definition (1) was used and the average values of curvature and torsion were obtained as

$$AC = 1/L \int_0^L \kappa(s) ds, AT = 1/L \int_0^L \tau(s) ds \quad (2)$$

Moreover, as global anatomic features of vascular segments, bending (BE) and twisting energy (TE), i.e., the energy required to bend and twist a straight line into its curved shape, were calculated as previously defined [18,19]:

$$BE = L^2 \int_0^1 \kappa^2(w) dw \quad (3)$$

$$TE = L^2 \int_0^1 \tau^2(w) dw$$

where $w=s/L$ is the normalized curvilinear abscissa.

Among geometric vascular attributes, cross-sectional area $A(s)$ along the vessel was also considered, where $A(s)$ was calculated automatically at the generic curvilinear abscissa s via intersection of a plane normal to the centerline at s location.

Computational Hemodynamics

For all the cases of interest, we solved the governing equations of fluid motion, where the fluid was assumed to be unsteady, incompressible, isothermal, homogeneous. In detail, in this application the Navier-Stokes equations in the form

$$\begin{cases} \rho(\partial_t \mathbf{u} + \mathbf{u} \cdot \nabla \mathbf{u}) + \nabla \cdot (\mu(\nabla \mathbf{u} + (\nabla \mathbf{u})^T)) + \nabla p = \mathbf{f}, \\ \nabla \cdot \mathbf{u} = 0 \end{cases} \quad (4)$$

where ρ is the density, μ the dynamic viscosity, \mathbf{u} the velocity and p the pressure, were numerically solved by applying the finite element method. In detail, the fluid domain was discretized by using tetrahedrons. The mesh generation was carried out using the tools available in the VMTK library, selecting elements with uniform edge length. For the considered geometries, mesh cardinality was about 6.6 millions of tetrahedrons. Here mixed P1bubble-P1 elements were used, which provide (1) piecewise continuous linear interpolation enriched by a cubic bubble (i.e., with null trace on the boundary of the tetrahedrons) for the velocity, (2) piecewise continuous linear approximation for the pressure. As well known, this choice guarantees that the discretization of the problem is nonsingular, i.e. solvable [20].

The Navier-Stokes equations were solved using the open source C++ library LifeV (www.lifev.org), a parallel Finite Element solver. As for the applied numerical scheme, the time integration was performed using a second order BDF scheme with an algebraic splitting of the velocity and pressure fields with a Yosida scheme with pressure corrections [21,22]. The convective effects were treated using a Streamline Diffusion approach [23].

As for boundary condition prescription, different strategies were applied, depending on the nature of the boundary. Phase-contrast MRI data were available, in terms of flow rate waveform, at a cross section slightly distal to the aortic valve in the one-year follow up case (denoted by CASE B in Fig.1). This flow rate waveform was applied at the inflow section of both CASE A and CASE B. As it is well known, flow rate conditions are “defective” since they are not enough for solving the Navier-Stokes equations and need to be completed either by simplifying assumptions or by special (and expensive) numerical techniques [24]. In particular, following a well-established procedure for ascending aorta, we postulated flat velocity inlet profiles with flow extensions added at the boundary sections to reduce the effect of the defective boundary conditions in the region of interest [25]. Average Reynolds number at the inflow sections was about 1240.

In the lack of measured outflow data, a classical three-element Windkessel model was postulated at each outlet section, modeling the impedance of the distal circulation. Technically, the peripheral impedance at each outflow section was represented by two resistances R1 and R2 and one compliance C (RCR model). The specific values of those parameters, applied both to Case A and Case B, were taken from [26]. The arterial walls were assumed to be non-porous and rigid, correspondingly null velocity conditions were enforced. Finally ρ and μ were set equal to 1060 kg/m^3 and 3.5 cP , respectively.

Hemodynamic Quantitative Description

The impact of the applied TEVAR on the aortic hemodynamics after implantation was evaluated by computing both the wall shear stress (WSS) distribution at the luminal surface (which is related to arterial disease) and the intravascular flow structures. Since the natural blood flow in aorta has been demonstrated to be helical [27-29] we actually focused on helical flow structures.

The presence of disturbed shear was investigated in terms of luminal distributions of two of the most widely used wall shear stress (WSS)-based descriptors, i.e., the Time-Averaged WSS (TAWSS) [30], and the Oscillatory Shear Index (OSI) [31]

$$\text{TAWSS} = \frac{1}{T} \int_0^T |\boldsymbol{\tau}_w(\mathbf{x}, t)| \cdot dt \quad (5)$$

$$\text{OSI} = 0.5 \left[1 - \frac{\left| \int_0^T \boldsymbol{\tau}_w(\mathbf{x}, t) \cdot dt \right|}{\int_0^T |\boldsymbol{\tau}_w(\mathbf{x}, t)| \cdot dt} \right] \quad (6)$$

where T is the overall interval of the cardiac cycle and \mathbf{x} is the position on the vessel wall. In general, low and oscillatory shear stress is considered athero-genic, whereas high shear stress is athero-protective [32].

As for the characterization of helical flow, by definition, the helicity $H(t)$ of a fluid flow confined to a domain \mathbf{D} of a 3D Euclidean space \mathbf{R}^3 is given by the integral value of the scalar product of the local velocity \mathbf{v} and the vorticity $\boldsymbol{\omega}$ vectors:

$$H(t) = \int_{\mathbf{D}} \mathbf{v}(\mathbf{x}, t) \cdot \boldsymbol{\omega}(\mathbf{x}, t) \, d\mathbf{x} \quad (7)$$

Being related to the magnitude of the nonlinear term in the Navier-Stokes equation, helicity is strongly related to the evolution and stability of both turbulent and laminar flows [33].

More recently, the non-dimensional Localized Normalized Helicity (LNH) defined as:

$$\text{LNH}(\mathbf{x};t) = \frac{\mathbf{v}(\mathbf{x};t) \cdot \boldsymbol{\omega}(\mathbf{x};t)}{|\mathbf{v}(\mathbf{x};t)| |\boldsymbol{\omega}(\mathbf{x};t)|} = \cos \varphi(\mathbf{x};t) \quad (8)$$

$$-1 \leq \text{LNH} \leq 1$$

has been applied more and more to cardiovascular fluid mechanics [15,16,34-38]. In fact, LNH is the local value of the cosine of the angle $\varphi(\mathbf{x};t)$ between the velocity and vorticity vectors: the absolute value of LNH ranges between one, when the flow is purely helical, and zero, in general, in presence of reflectional symmetry in the flow. Moreover, the sign of LNH is a useful indicator of the direction of rotation. As a matter of fact, LNH describes the changes in the direction of the rotation of flow inside vessels during the cardiac cycle, because a local right/left-handed rotation can be identified by a change in sign of the local value of LNH.

Results

Geometric Description

Local curvature and torsion profiles calculated along models before and at two different stages after stent-graft implantation procedure by applying (1) provide a clear representation of the impact that the stenting procedure has in reshaping the vessel. Figures 1 and 2 show how the severity of curvature and non-planarity along the vessel does vary as a consequence of the presence of the stent-graft, also highlighting their complex nature and non-uniformity. In particular it can be noticed that:

- the overall effect of the implantation is a modification of the local value of the curvature of the aorta (Figures 1 and 2), in particular in the segment of the aortic arch immediately downstream of the supra-aortic vessels. On the opposite, average aortic curvature does not vary as a consequence of the implantation (Table 1);
- overall, both average and pointwise values of aortic non-planarity are affected by stent-graft implantation (Table 1). In detail, the pre-op case (CASE 0) features a bi-modal torsion (with peaks of -3mm^{-1} in the descending aorta, Figure 2), while CASE A shows a uni-modal tortuosity with a

peak value in the opposite direction (opposite torsion). Notably, no peak values for torsion are evident at the late observational stage (CASE B).

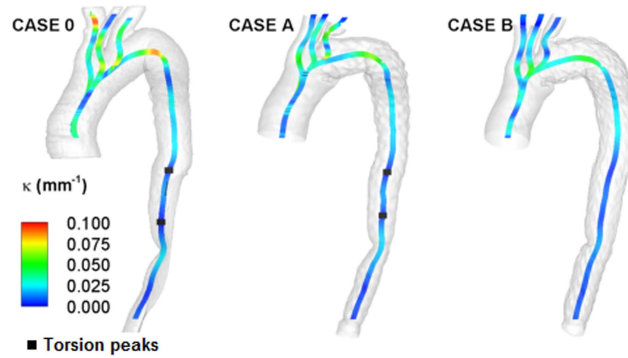


Figure 1 - Three-dimensional reconstruction of pre-operative aorta (CASE 0), post-operative aorta immediately after the surgery (CASE A), and post-operative aorta one year after the surgical intervention (CASE B). Vessels centerline, color-coded with local values of curvature κ , and location of torsion τ peak values are also presented.

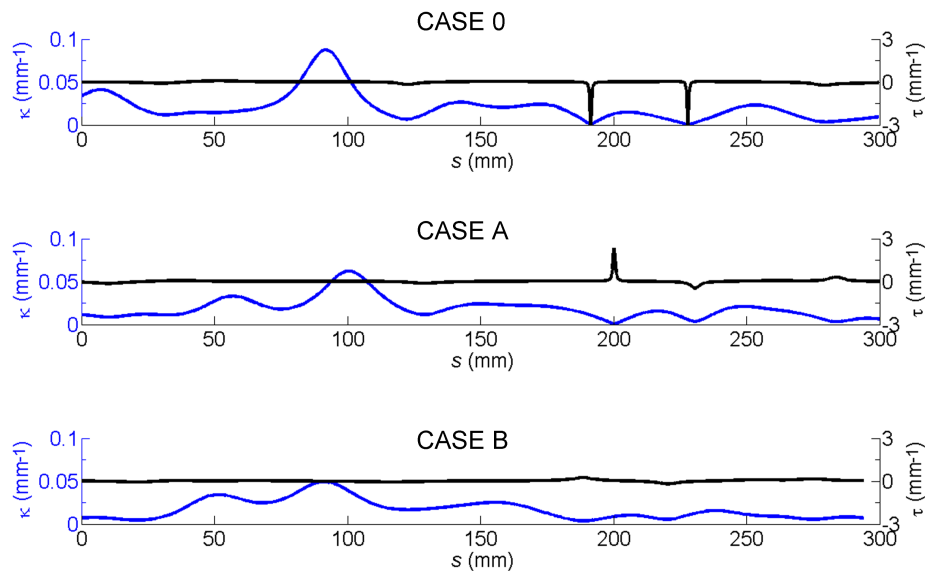


Figure 2 - Aortic longitudinal profiles of curvature κ and torsion τ . The varying severity of curvature and torsion along vessels highlights the remodelling of the pre-operative aorta (CASE 0), occurring in the post-operative aorta immediately after (CASE A) and one year after surgery (CASE B) as a consequence of stent-graft implantation.

Table 1 – Geometric analysis of the centerline of pre-operative aorta (CASE 0), post-operative aorta immediately after the surgery (CASE A), and post-operative aorta one year after the surgical intervention (CASE B). The main geometric attribute of the vessel is characterized in terms of average values curvature and torsion, bending and twisting energy

<i>AORTA</i>	Average Curvature (mm ⁻¹)	Average Torsion (mm ⁻¹)	Bending Energy (J)	Twisting Energy (J)
CASE 0	0.017	-0.047	0.0044	0.5991
CASE A	0.017	0.014	0.0038	0.1716
CASE B	0.015	0.018	0.0028	0.0417

The aortic remodelling occurring after the stent-graft implantation is highlighted by the analysis of the correlation between centerline features along the observational window. In particular, Table 2 points out that (1) a moderate correlation still persists for the aortic curvature between pre and post-implantation, (2) on the contrary, correlation is very poor (if not negative) for torsion. These results are confirmed by the analysis summarized in Table 1, where it can be observed how both the bending and twisting energy averaged along the aorta are progressively reduced from pre-to-post observation (from CASE 0 to CASE B), as a consequence of the stent-graft implantation.

Table 2 - Analysis of the correlation of centerline features (in terms of correlation coefficient) along the observational window going from the pre-operative stage (CASE 0) through the post-operative immediately after the surgery (CASE A), to the post-operative aorta stage one year after the surgical intervention (CASE B).

Correlation coefficient r ($p < 0.01$)	CURVATURE		TORSION	
	CASE A	CASE B	CASE A	CASE B
<i>AORTA</i>				
<i>PRE</i>	0.623	0.693	0.024	-0.107
<i>EARLY</i>	-	0.760	-	0.256

The analysis of the variation of the cross-sectional area along the aorta (Figure 3), limited to the stented region, clearly shows that (1) the presence of the stent-graft leads to progressively restore more physiologic cross-sectional area values both in the proximal (cross-sectional area reduction) and in the distal part (cross-sectional area augmentation) of the stented segment; (2) from immediately after the stent-graft implantation (CASE A) to one year (CASE B) after the intervention, the aorta undergoes an almost uniform expansion, with the variation in the cross-sectional area showing a similar trend ($r = 0.94$, $p < 0.01$) along the vessel. Notably, the stent-graft implantation has also a positive effect in enlarging the marked lumen reduction which is present at the pre-operative stage (CASE 0), affecting the distal tract of the diseased descending aorta.

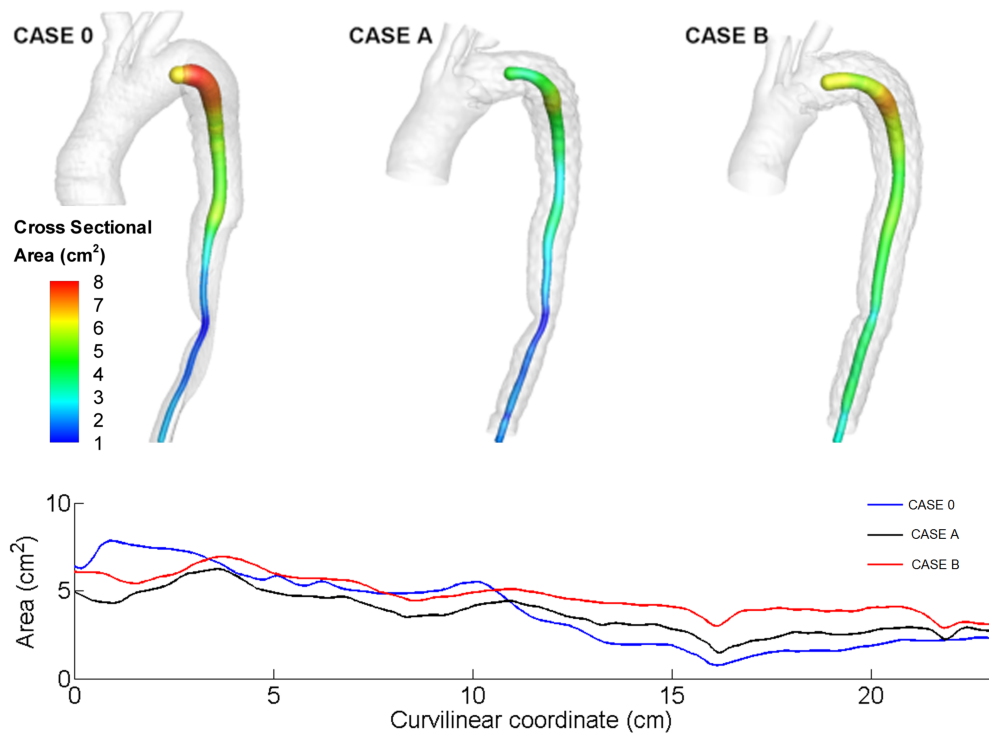


Figure 3 - Visualization of the variation of the cross-sectional area along the aorta from the pre-operative (CASE 0) to the post-operative stages immediately after (CASE A) and one year after surgery (CASE B). The longitudinal profiles of the aortic cross-sectional area are also presented.

Hemodynamic Description

The snapshot of the intravascular flow field provided by the peak systolic instantaneous streamlines clearly highlight more regular fluid structures after one year from implantation (Figure 4) in (1) the proximal segment of the stented artery, immediately downstream of branching of the left subclavian artery from the

aorta; (2) the distal segment of the descending aorta, where a marked lumen reduction was present before stent-graft implantation; (3) the proximal regions of the left carotid artery and of the left subclavian artery.

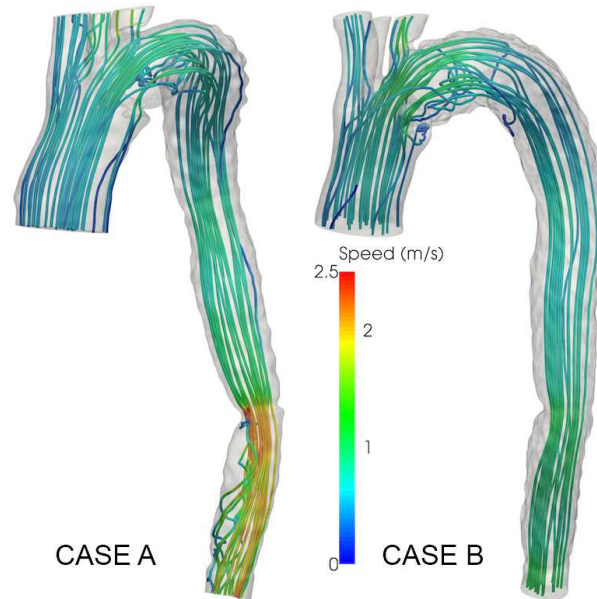


Figure 4 - Snapshot of the intravascular flow field, in terms of instantaneous streamlines at peak systole, in the post-operative aorta immediately after (CASE A) and one year after surgery (CASE B). Instantaneous streamlines are coloured by the local velocity vector magnitude.

The impact of the implantation on aortic intravascular flow was also investigated more in depth by visualizing LNH isosurfaces (defined by equation (8)) of flow fields averaged in time along the systole and diastole, respectively. Adopting threshold values of LNH (± 0.3) for the visualization of counter-rotating helical blood flow structures (positive and negative LNH values indicate counter-rotating helical structures in Figure 5), the presence of different topological features can be observed for CASE A and CASE B. In particular, Figure 5 shows that along the systole more “large and organized” counter-rotating fluid structures characterize the aortic flow in the distal segment of the aortic arch and in the descending aorta of CASE A than in CASE B. However, based on previous *in vivo* [28,29] and *in silico* observations [16,25], helical flow structures seems to be still less coherent at one year from implantation, than healthy human aortas.

In diastole, the helical structures appear as less organized than in systole in the entire aortic volume (Figure 5) at the two different post-interventional stages (according to recent observations [16]), with CASE B presenting coherent helical flow structures in the descending aorta larger than CASE A.

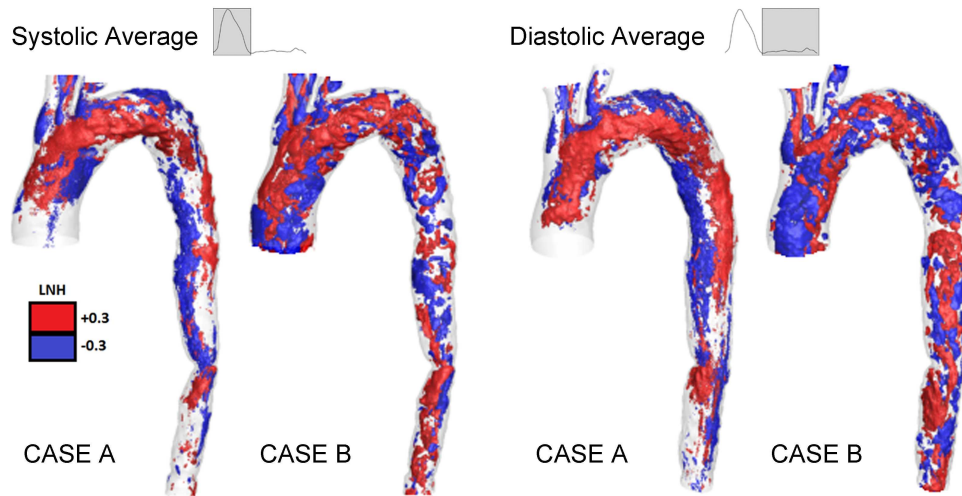


Figure 5 - Helical flow structures in the post-operative aorta immediately after (CASE A) and one year after surgery (CASE B). For both cases, isosurfaces of LNH (± 0.3) averaged over systole and diastole are presented. Counter-rotating helical flow structures can be observed (left-handed, negative LNH value; right-handed, positive LNH value).

The analysis of the distribution of the WSS-based descriptors shows that, in consequence of the geometric remodelling (Figure 6) (1) the luminal surface exposed to low WSS (less than 0.4 Pa [32]) at the ascending aorta is wider in CASE B than in CASE A; (2) inside the stent-graft region, where low WSS distribution identify regions more prone to thrombus formation, the surface area exposed to low WSS is larger in the arch extrados in CASE A and larger in the grafted descending aorta segment in CASE B, the latter presenting a low WSS region localized in the region of the stenosis; (3) in CASE B presence of oscillatory WSS in the ascending aorta is reduced (Figure 7). The latter circumstance is confirmed by the fact that in the aortic segment proximal to the implanted stent-graft, the luminal surface featuring $OSI > 0.4$ is diminished in comparison to CASE A.

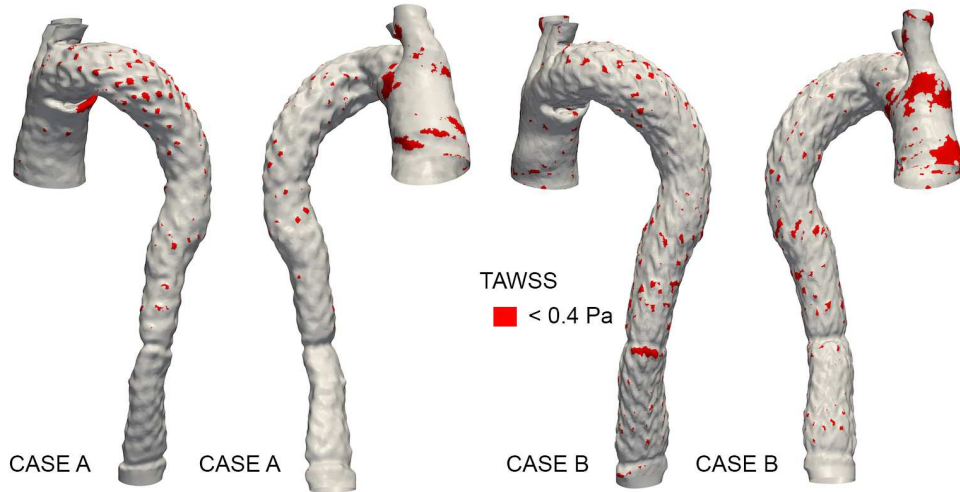


Figure 6 – Surface area exposed to low time-averaged WSS (TAWSS < 0.4 Pa) in the post-operative aorta immediately after (CASE A) and one year after surgery (CASE B). The luminal surface exposed to low WSS at the ascending aorta identifies more atherosusceptible regions. Inside the stent-graft region, low WSS identifies regions more prone to thrombus formation.

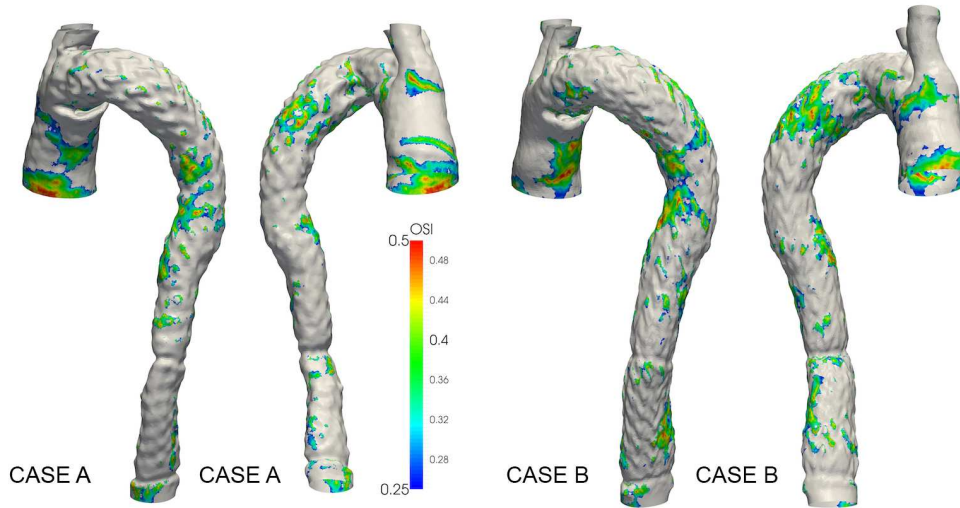


Figure 7 - Surface area exposed to high oscillatory WSS (OSI > 0.25) in the post-operative aorta immediately after (CASE A) and one year after surgery (CASE B).

Discussion

As recently reported, technological advancements and the growing experience with endovascular interventions have resulted in a progressively increasing utilization for TEVAR [40]. In particular, TEVAR has become alternative to open surgery in patients with a high operative risk, and in acutely unstable patients

to achieve rapid aortic stabilization. However, the use of TEVAR is associated to the risk of complications that may require, e.g., endovascular or open surgical interventions [40]. In this sense, the use of quantitative morphometry combined with a detailed analysis of local hemodynamics could (1) enrich the monitoring of medium and long term outcome of patients undergoing TEVAR and, eventually, (2) support clinical decision when stent-graft complication after primary TEVAR require secondary surgical and/or interventional procedures.

The coupling of medical imaging with CFD has been recently applied to obtain realistic, detailed descriptions of the perturbation of the local hemodynamics as a consequence of TEVAR procedure [7], in particular to get insight into the hemodynamic consequences of the bird-beak effect [7,9,10]. In parallel, the application of imaging tools for TEVAR preoperative screening and follow up has been recently proposed [4,5,7-11,42].

Here we combine quantitative aortic morphometry and multiscale computational hemodynamics for a detailed analysis of the impact of TEVAR procedure both on aortic remodelling and local hemodynamics in a follow up study up to one year from the intervention. Our findings show that after endovascular repair, in the analysed subject: (1) late aortic remodelling persists not only in the stented segment, but in the whole thoracic aorta, with changes in local aortic curvature and non-planarity (Figures 1 and 2), as confirmed by the progressive reduction of the bending and twisting energy averaged along the aorta during the follow up (Table 1) and the progressive restore of more physiological cross-sectional areas (Figure 3); (2) the aortic hemodynamics progressively turn back to more physiological flow patterns (Figure 4), even if the physiological intravascular helical blood flow structures have still not been re-established after one year (Figure 5); (3) at the ascending aorta the remodelling has not clear beneficial effects in reducing the luminal surface exposed to low and oscillatory WSS (Figure 6) and the same holds for the associated flow shaping occurring between the stent-graft implantation and one year follow up; (4) in the stented segment near-wall low velocity regions (corresponding to low TAWSS, Figure 6) are still present in CASE B, suggesting that risk of thrombosis inside the graft still persist; (5) as a consequence of stent-graft implantation, the presence of a stenosis in the descending aorta is only partially solved after one year, indicating that its presence could still be the source of secondary complications.

There are several limitations that could weaken the findings of this study. First of all, the use of the same inflow boundary condition, which is specific of CASE B, also for CASE A, being phase-contrast MRI data not available immediately after the stent-graft implantation. As this could be a major limitation for this study, here we evaluated the sensitivity of the aortic hemodynamics immediately after implantation (CASE A) with respect to changes in input flow rate waveform shapes and inlet flow rate mean value. In detail, (1) a flow rate waveform previously measured at the ascending aorta [26], and (2) flow rate waveforms with average values equal to $\pm 10\%$ of the average flow rate measured at one year from implantation (CASE B) were prescribed at the inflow section of CASE A. However, our results showed that the near-wall hemodynamics of CASE A is not markedly affected by different flow rate waveforms shape and average values imposed at the inflow section, the WSS-based descriptors maintaining unchanged patterns at the luminal surface (data not shown).

Other limitations could affect our findings. The fact that flow rate measured data used as conditions at the ascending aorta inflow boundary are defective [25] and have been arbitrarily completed by the assumption of a flat inlet profile may affect the final results and this nonlinearly combines with the assumptions and parameter uncertainty on outflow boundary conditions [43], blood rheology [44], the distensibility of the aortic wall [8] (even if it is worth noting that the presence of the stent-graft is expected to make the aorta stiffer [36]), the reconstruction of the anatomic models. Altogether these assumptions could bias the results in an overall significant way. However, all those limitations do not limit the generality of the approach here proposed, which can be made more and more patient-specific resorting to more mathematically sound data assimilation methods [46,47] and integrating further information from clinical imaging (e.g., measured three-dimensional phase velocity profiles at inflow boundaries [16,25] and measured wall distensibility [8]).

In conclusion, the findings of this study clearly show that combining vascular imaging of the thoracic aorta and multiscale computational hemodynamics is a promising reliable patient-specific tool which could improve TEVAR clinical understanding, management and follow-up.

Acknowledgments

The authors acknowledge the computational resources provided by the project 'Patient Specific Computational Analysis of Aortic hemodynamics over Large data sets (PASCA2L)', LISA (Interdisciplinary Laboratory for Advanced Simulation) Action (Region Lombardy and CINECA consortium, Italy).

Moreover, DG and UM were supported by a personnel award from Joint Project for the Internationalization of Research 2014 from Compagnia di San Paolo Foundation and Politecnico di Torino. FA, MC, AL, SM, AV, AR were partially supported by the Cariplo Foundation through the iCardioCloud Project. FA, MC, SM, AR were partially supported by the European Research Council through the FP7 Ideas Starting Grant (grant no. 259229) ISOBIO - Isogeometric Methods for Biomechanics. This support is gratefully acknowledged.

References

- [1]. Sampson UK, Norman PE, Fowkes FGR, Aboyans V, Song Y, Harrell FE, Forouzanfar MH, Naghavi M, Denenberg JO, McDermott MM, Crigui MH, Mensah GA, Ezzati M, Murray C. Estimation of global and regional incidence and prevalence of abdominal aortic aneurysms 1990 to 2010. *Glob Heart* 2014;9(1):159-170.
- [2]. Steuer J, Björck M, Sonesson B, Resch T, Dias N, Hultgren R, Tunesi R, Wanhainen A, Lachat M, Pfammatter T. Editor's Choice–Durability of endovascular repair in blunt traumatic thoracic aortic injury: long-term outcome from four tertiary referral centers. *Eur J Vasc Endovasc Surg* 2015;50(4):460-465.
- [3]. Ueda T, Fleischmann D, Dake MD, Rubin GD, Sze DY. Incomplete endograft apposition to the aortic arch: bird-beak configuration increases risk of endoleak formation after thoracic endovascular aortic repair. *Radiology* 2010;255(2):645–652.
- [4]. Midulla M, Moreno R, Negre-Salvayre A, Nicoud F, Pruvo JP, Haulon S, Rousseau H. Impact of endografting on the thoracic aortic anatomy: comparative analysis of the aortic geometry before and after the endograft implantation. *Cardiovasc Intervent Radiol* 2014;37(1):69-76.
- [5]. Auricchio F, Conti M, Ferrazzano C, Sgueglia GA. A simple framework to generate 3D patient-specific model of coronary artery bifurcation from single-plane angiographic images. *Comput Biol Med* 2014;44:97-109.
- [6]. Choi G, Cheng CP, Wilson NM, Taylor CA. Methods for quantifying three-dimensional deformation of arteries due to pulsatile and nonpulsatile forces: implications for the design of stents and stent grafts. *Ann Biomed Eng* 2009;37(1):14-33.
- [7]. Auricchio F, Conti M, Lefieux A, Morganti S, Reali A, Sardanelli F, Secchi F, Trimarchi S, Veneziani A. Patient-specific analysis of post-operative aortic hemodynamics: a focus on thoracic endovascular repair (TEVAR). *Comput Mech* 2014;54:943-53.
- [8]. Midulla M, Moreno R, Baali A, Chau M, Negre-Salvayre A, Nicoud F, Pruvo JP, Haulon S, Rousseau H. Haemodynamic imaging of thoracic stent-grafts by computational fluid dynamics (CFD): presentation of a patient-specific method combining magnetic resonance imaging and numerical simulations. *Eur Radiol* 2012;22(10):2094-102.
- [9]. Rinaudo A, Raffa GM, Scardulla F, Pilato M, Scardulla C, Pasta S. Biomechanical implications of excessive endograft protrusion into the aortic arch after thoracic endovascular repair. *Comput Biol Med* 2015;66:235-241.
- [10]. van Bogerijen GH, Auricchio F, Conti M, Lefieux A, Reali A, Veneziani A, Tolenaar JL, Moll FL, Rampoldi V, Trimarchi S. Aortic hemodynamics after thoracic endovascular aortic repair, with particular attention to the birdbeak configuration. *J Endovasc Ther* 2014;21:791-802.
- [11]. van Bogerijen GH, van Herwaarden JA, Conti M, Auricchio F, Rampoldi V, Trimarchi S, Moll FL. Importance of dynamic aortic evaluation in planning TEVAR. *Ann Cardiothorac Surg* 2014;3(3):300-306.
- [12]. Yushkevich P, Piven J, Hazlett H, Smith R, Ho S, Gee J, Gerig G. User-guided 3D active contour segmentation of anatomical structures: significantly improved efficiency and reliability. *NeuroImage* 2006;31(3):1116–1128.
- [13]. Antiga L, Steinman DA. Robust and objective decomposition and mapping of bifurcating vessels. *IEEE Trans Med Imaging*. 2004;23(6):704-13.
- [14]. Sangalli LM, Secchi P, Vantini S, Veneziani A. Efficient estimation of three-dimensional curves and their derivatives by free-knot regression splines, applied to the analysis of inner carotid artery centrelines. *Appl Statist* 2009;58(3):285–306.
- [15]. Gallo D, Steinman DA, Morbiducci U. An insight into the mechanistic role of the common carotid artery on the hemodynamics at the carotid bifurcation. *Ann Biomed Eng* 2015;43(1):68-81.
- [16]. Morbiducci U, Gallo D, Cristofanelli S, Ponzini R, Deriu MA, Rizzo G, Steinman DA. A rational approach to defining principal axes of multidirectional wall shear stress in realistic vascular geometries, with application to the study of the influence of helical flow on wall shear stress directionality in aorta. *J Biomech* 2015;48:899-906.
- [17]. Zhou S, Shen X. Spatially adaptive regression splines and accurate knot selection schemes. *JASA* 2001;96(453):247–259.
- [18]. Meng S, Geyer SH, Costa LdF, Viana MP, Weninger WJ. Objective characterization of the course of the parasellar internal carotid artery using mathematical tools. *Surg Radiol Anat* 2008;30:519–526.

- [19]. Bogunovic H, Pozo JM, Cárdenes R, Villa-Uriol MC, Blanc R, Piotin M, Frangi AF. Automated landmarking and geometric characterization of the carotid siphon. *Med Image Anal* 2012;16(4):889–903.
- [20]. Arnold DN, Brezzi F, Fortin M, A stable finite element for the stokes equations, *Calcolo* 1984;21(4):337–344.
- [21]. Saleri F, Veneziani A. Pressure correction algebraic splitting methods for the incompressible Navier–Stokes equations. *SIAM J Numer Anal* 2005;43(1):174–194.
- [22]. Villa U. Scalable efficient methods for incompressible fluid-dynamics in engineering problems. Ph.D. thesis, Emory University, 2012.
- [23]. Elman D, Silvester H, Wathen A, Finite elements and fast iterative solvers with applications in incompressible fluid dynamics. 2005, Oxford University Press.
- [24]. Quarteroni A, Veneziani A, Vergara C. Geometric multiscale modeling of the cardiovascular system, between theory and practice. Technical Report Emory Math & CS TR-2015-007 2015; www.mathcs.emory.edu/reports.php
- [25]. Morbiducci U, Ponzini R, Gallo D, Bignardi C, Rizzo G. Inflow boundary conditions for image-based computational hemodynamics: impact of idealized versus measured velocity profiles in the human aorta. *J Biomech* 2013;46(1):102–109.
- [26]. Kim H, Vignon-Clementel I, Figueroa C, LaDisa J, Jansen K, Feinstein J, Taylor C. On coupling a lumped parameter heart model and a three-dimensional finite element aorta model. *Ann Biomed Eng* 2009;37(11):2153–2169.
- [27]. Kilner PJ, Yang GZ, Mohiaddin RH, Firmin DN, Longmore DB. Helical and retrograde secondary flow patterns in the aortic arch studied by three-directional magnetic resonance velocity mapping. *Circulation* 1993;88:2235–2247.
- [28]. Morbiducci U, Ponzini R, Rizzo G, Cadioli M, Esposito A, De Cobelli F, Del Maschio A, Montevicchi FM, Redaelli A. In Vivo Quantification of helical blood flow in human aorta by time-resolved three-dimensional cine phase contrast MRI. *Ann Biomed Eng* 2009;37(3):516–531.
- [29]. Morbiducci U, Ponzini R, Rizzo G, Cadioli M, Esposito A, Montevicchi FM, Redaelli A. Mechanistic insight into the physiological relevance of helical blood flow in the human aorta. An in vivo study. *Biomech Model Mechanobiol* 2011;10:339–355.
- [30]. Caro CG, Fitz-Gerald JM, Schroter RC. Atheroma and arterial wall shear: Observation, correlation and proposal of a shear dependent mass transfer mechanism for atherogenesis. *Proc R Soc Lond [Biol]* 1971;117:109–159.
- [31]. Ku DN, Giddens DP, Zarins CK, Glagov S. Pulsatile flow and atherosclerosis in the human carotid bifurcation. Positive correlation between plaque location and low oscillating shear stress. *Arteriosclerosis* 1985;5:293–302.
- [32]. Malek AM, Alper SL, Izumo S. Hemodynamic shear stress and its role in atherosclerosis. *JAMA* 1999;282:2035–42.
- [33]. Moffatt HK, Tsinober A. Helicity in laminar and turbulent flow. *Annu Rev Fluid Mech* 1992;24:281–312.
- [34]. Gallo D, Steinman DA, Bijari PB, Morbiducci U. Helical flow in carotid bifurcation as surrogate marker of exposure to disturbed shear. *J Biomech* 2012;49(14):2398–2404.
- [35]. Morbiducci U, Ponzini R, Grigioni M, Redaelli A. Helical flow as fluid dynamic signature for atherogenesis in aortocoronary bypass. A numeric study. *J Biomech* 2007;40(3):519–534.
- [36]. Brown, AG, Yubing S, Marzo A, Staicu C, Valverde I, Beerbaum P, Lawford PV, Hose DR. Accuracy vs. computational time: translating aortic simulations to the clinic. *J Biomech* 2012;45:516–523.
- [37]. Liu X, Sun A, Fan Y, Deng X. Physiological significance of helical flow in the arterial system and its potential clinical applications. *Ann Biomed Eng* 2015;43:3–15.
- [38]. Aristokleous N, Seimenis I, Georgiou GC, Nicolaidis A, Anayiotos AS. The effect of head rotation on the geometry and hemodynamics of healthy vertebral arteries. *Ann Biomed Eng* 2015;43(6):1287–97.
- [39]. Aristokleous N, Seimenis I, Georgiou GC, Papaharilaou Y, Brott BC, Nicolaidis A, Anayiotos AS. Impact of head rotation on the individualized common carotid flow and carotid bifurcation hemodynamics. *IEEE J Biomed Health Inform.* 2014;18(3):783–9.
- [40]. Nozdrzykowski M, Luehr M, Garbade J, Schmidt A, Leontyev S, Misfeld M, Mohr FW, Etz CD. Outcomes of secondary procedures after primary thoracic endovascular aortic repair. *Eur J Cardiothorac Surg* 2015; doi:10.1093/ejcts/ezv279.

- [41]. Hsu HL, Chen CK, Chen PL, Chen IM, Hsu CP, Chen CW, Shih CC. The impact of bird-beak configuration on aortic remodeling of distal arch pathology after thoracic endovascular aortic repair with the Zenith Pro-Form TX2 thoracic endograft. *J Vasc Surg* 2014;59(1):80-8.
- [42]. Kotelis D, Brenke C, Wörz S, Rengier F, Rohr K, Kauczor HU, Böckler D, von Tengg-Kobligk H. Aortic morphometry at endograft position as assessed by 3D image analysis affects risk of type I endoleak formation after TEVAR. *Langenbecks Arch Surg*. 2015;400(4):523-9.
- [43]. Gallo D, De Santis G, Negri F, Tresoldi D, Ponzini R, Massai D, Deriu MA, Segers P, Verheghe B, Rizzo G, Morbiducci U. On the use of in vivo measured flow rates as boundary conditions for image-based hemodynamic models of the human aorta. Implications for indicators of abnormal flow. *Ann Biomed Eng* 2012;40(3):729-741.
- [44]. Liu X, Fan Y, Deng X, Zhan F. Effect of non-newtonian and pulsatile blood flow on mass transport in the human aorta. *J Biomech* 2011;44:1123–1131.
- [45]. Conrad MF, Carvalho S, Ergul E, Kwolek CJ, Lancaster RT, Patel VI, Cambria RP. Late aortic remodeling persists in the stented segment after endovascular repair of acute complicated type B aortic dissection. *J Vasc Surg*. 2015;62(3):600-605.
- [46]. D’Elia M, Perego M, Veneziani A. A variational data assimilation procedure for the incompressible Navier–Stokes equations in hemodynamics. *J Sci Comput* 2012;52:340–59.
- [47]. Bertagna L, D’Elia M, Perego M, Veneziani A. Data Assimilation in Cardiovascular Fluid–Structure Interaction Problems: An Introduction. In *Fluid-Structure Interaction and Biomedical Applications*, 2014; 395-481. Springer Basel.